# Understanding the Growth Mechanisms of Ag Nanoparticles Controlled by Plasmon-Induced Charge Transfers in Ag-TiO 2 Films

**10 AUTHORS**, INCLUDING:

Nathalie Destouches
Université Jean Monnet
**147** PUBLICATIONS **477** CITATIONS

SEE PROFILE

Lefkir Yaya
French National Centre for Scientific Research
**37** PUBLICATIONS **415** CITATIONS

SEE PROFILE

Said Bakhti
Université Jean Monnet
**18** PUBLICATIONS **16** CITATIONS

SEE PROFILE

Musahid Ahmed
Lawrence Berkeley National Laboratory
**128** PUBLICATIONS **2,332** CITATIONS

SEE PROFILE

# Understanding the Growth Mechanisms of Ag Nanoparticles Controlled by Plasmon-Induced Charge Transfers in Ag-TiO2 Films

Zeming Liu,[†] Nathalie Destouches,*,[†] Guy Vitrant,*,[‡] Yaya Lefkir,[†] Thierry Epicier,[§] Francis Vocanson,[†] Saïd Bakhti,[†] Yigang Fang,[‖] Biswajit Bandyopadhyay,[‖] and Musahid Ahmed[‖]

[†]Université de Lyon, CNRS, UMR 5516, Laboratoire Hubert Curien, Université Jean-Monnet, 18 Rue Pr. Lauras, F-42000 Saint-Etienne, France

[‡]IMEP-LAHC, Minatec, Grenoble-INP, CNRS-UMR 5130, 3 Parvis Louis Néel-CS 50257, F-38016 Grenoble, France

[§]MATEIS, UMR 5510 CNRS, Université de Lyon, INSA-Lyon, 7 Avenue Jean Capelle, F-69621 Villeurbanne, France

[‖]Chemical Sciences Division, Lawrence Berkeley National Laboratory, Berkeley, California 94720, United States

**S** *Supporting Information*

**ABSTRACT:** Mesoporous thin films of TiO2 doped with silver can undergo spectacular microstructural modifications upon laser scanning at visible wavelengths through the excitation of a localized surface plasmon resonance in Ag nanoparticles (NPs). The latter can result in competitive physicochemical mechanisms, leading either to the shrinkage or to the growth of NPs depending on the exposure conditions. Contrary to intuition, we provide evidence that the speed of the laser scan controls the size of NPs as follows: low speeds lead to silver oxidation and a decrease in the NP size, whereas high speeds induce rapid temperature rises and a



spectacular growth of NPs. Both regimes are separated by a speed threshold that depends on extrinsic and intrinsic parameters such as laser power, beam diameter, and initial size of Ag NPs. We propose here a comprehensive model based on a set of coupled differential equations describing the transformations of silver under laser excitation between the $Ag^0$, $Ag^+$, and metallic NP states, which provides a convincing physicochemical explanation of the experimental findings. This study constitutes a significant advance in the understanding of oxidation−reduction processes involved during laser exposure of metallic NPs and opens new directions to control their growth rate and their final size.
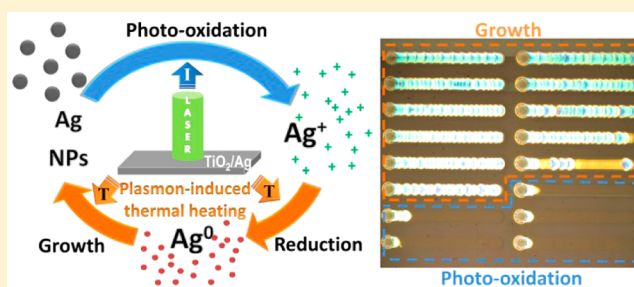
## INTRODUCTION

Plasmon-induced charge transfer[1,2] occurring at metal−semiconductor interfaces in porous TiO2 containing silver or gold nanoparticles (NPs) promises novel applications in photocatalysis[3−9] and photovoltaics.[2,10−14] Noble metal NPs are mainly used to extend the photoresponse of TiO2 to the visible and near-infrared spectral ranges through the injection of "hot electrons" in the semiconductor. Highly energetic electrons can indeed escape the conduction band of metal NPs after light absorption and decay of the localized surface plasmon that transfers its energy to "hot electrons". The latter are efficiently collected outside the metal, due to the Schottky barrier formed at the interface with TiO2. However, the size and shape of NPs appear to strongly influence the carriers' injection yield.[15−17]

Periodic arrays of metal NPs are used to improve the absorption efficiency of materials, which in turn increases "hot electron" injection. Such devices couple light into photonic modes propagating in the semiconductor layer to confine light and increase its interaction with matter.[18] Coupling both approaches would lead to the formation of periodic arrays of metal NPs in TiO2 films. These nanostructures were recently obtained through a laser-induced self-organization process.[19]

We demonstrated that self-organized gratings of silver NPs could be produced in TiO2 thin films in a versatile and stable process, where a single visible laser beam scans the film surface. The resulting structures were shown to act as resonators trapping light at various wavelengths into the films. The motivation of the present study is to understand the physicochemical reactions that influence the self-organization process and lead to nanoparticle formation. This is of paramount importance for optimizing the nanostructures and especially the final nanoparticle size because these control both "hot electron" generation and the coupling efficiency of the resonant grating.

When exposed to visible light, silver NPs sustain a localized surface plasmon resonance (LSPR) whose decay occurs on a femtosecond time scale either radiatively by photon emission[20] or nonradiatively by excitation of "hot electrons".[21,22] "Hot electrons" with energies higher than the Schottky barrier can be injected into the semiconductor, leading to positively charged

nanoparticles.[23] Tunneling through the barrier can also occur with a smaller probability.[24] In these cases, the ionized silver NPs are not stable anymore and tend to dissolve into $Ag^+$ ions.[25] This effect is especially known to give rise to multicolor photochromism by selective oxidation of certain sizes of NPs under monochromatic light.[26−29] The remaining photoexcited electrons relax through electron−electron and electron−phonon collisions and are ultimately converted into heat.[30] It has been established experimentally that when the heating that impacts the surrounding matrix is high enough, reduction and aggregation phenomena also take place and silver NPs can grow.[19,31] Plasmon absorption can therefore result in two opposite effects whose competition governs the evolution of the nanoparticle size during exposure.

In this paper, we demonstrate how the intensity distribution of the laser beam scanning the sample at a constant speed determines the relative weight of oxidation, reduction, and aggregation processes during exposure and how these processes influence the final size of silver nanoparticles. We show a counterintuitive experimental result where thermally induced growth of silver nanoparticles only occurs for high scanning speeds and compare it to a model to simulate the changes in the nanoparticle size versus time during the beam passage. This model links the density and size of metallic silver nanoparticles, the concentration of reduced silver atoms ($Ag^0$) and the concentration of silver ions ($Ag^+$) in the system.

## ■ EXPERIMENTAL SECTION

Experiments are carried out on mesoporous films of amorphous $TiO_2$ loaded with silver salt and deposited on glass substrates. The elaboration process has already been reported in several of our previous articles.[19,31−35] The pore size of the films ranges from 5 to 20 nm, and their thickness is estimated to $230 \pm 50$ nm. Ionic silver is introduced by soaking the samples in an aqueous ammoniacal silver nitrate solution.[31−35] Silver ions spontaneously reduce and aggregate to form very small nanoparticles less than 3 nm in diameter after 12 h of drying in the dark at room temperature. In its initial state, before exposure to visible light, the sample contains three forms of silver: silver ions ($Ag^+$), reduced silver atoms ($Ag^0$), and silver NPs, whose relative concentrations are unknown. The relative concentration of the reduced species can, however, be increased using the photocatalytic behavior of $TiO_2$, i.e., injection of electrons from $TiO_2$ into Ag under UV light irradiation.[26−29] In this work, we consider two samples with different initial states: one obtained after simple drying for 12 h (sample I1) and the other dried in the same conditions then exposed to UV light (400 $\mu$W·cm$^{-2}$ at 254 nm wavelength) for 30 min (sample I2). The NP size and density were obtained from high angle annular dark field scanning transmission electron microscopy (HAADF-STEM, TEM, Jeol 2010F) micrographs. A quantitative analysis of the HAADF intensity derived from previous works[36,37] was used together with image processing to accurately identify and characterize small silver NPs within the inhomogeneous background intensity due to the mesoporosity of $TiO_2$.

Laser exposures were carried out at 488 nm with a continuous wave (CW) Ar−Kr ion laser (Coherent Innova i70) because this wavelength lies in the LSPR band of silver NPs and is not absorbed by $TiO_2$.[31] The laser beam, whose intensity distribution can be described by a 2D Gaussian function, was slightly focused on the sample surface with a 10× microscope objective (Olympus MPlan N, N.A. 0.25) under normal incidence to a circular spot with a diameter of 12.8 $\mu$m

in the focal plane at $1/e^2$ in intensity. A slight focusing of the laser light was required to increase the intensity on the sample for chemistry to occur. The sample was placed on a motorized translation stage and could move at constant speed in the $x$ and $y$ directions (Figure 1). Moving the sample in the $z$ direction
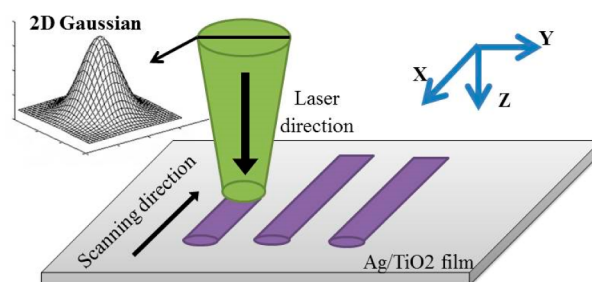


**Figure 1.** Sketch of exposure conditions. A CW visible laser is slightly focused on the sample, which moves at a constant speed along the scanning direction. The laser beam forms a circular spot on the sample surface and has a Gaussian shape intensity distribution.

changed the laser focusing and hence the beam diameter on the sample surface. This resulted in a variation of the incident intensity. The output power of the laser could also be varied. It must be noted that varying the beam diameter or the laser power to set the incident intensity on the sample surface was not equivalent. Indeed, the NP growth strongly depends on temperature, which varies with beam diameter even when the intensity is fixed due to heat dissipation. Hence we report both beam diameter and incident laser power.

## ■ RESULTS AND DISCUSSION

**Oxidation versus Growth: The Scanning Speed as a Crucial Parameter.** Light-induced oxidation of silver nanoparticles embedded in $TiO_2$ matrix as reported in the literature occurs even at low light intensity.[26−28,33,34] The NP shrinking rate increases with higher intensity and at wavelengths with greater absorption. The growth of silver nanoparticles is expected to be induced thermally and is only observed at a high threshold intensity. We performed a set of experiments to determine the minimum intensity required to observe the NP growth. We fixed the beam diameter to minimum (laser focused on the sample surface), performed exposures of 1 s (static exposure), and we varied the incident laser power until a dramatic color change (a dot) on the sample was observed, as observed at the beginning of each line in Figure 2. The color change is sharp; below the power threshold there is no effect, above the threshold a colored dot appears. The measured power threshold does not depend on the exposure time from
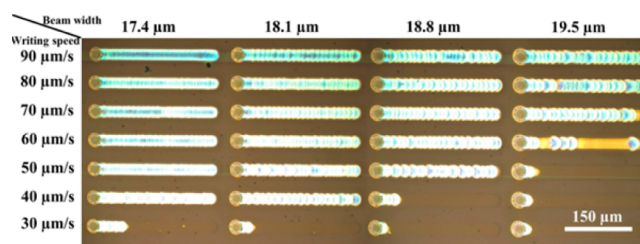


**Figure 2.** Optical microscopy pictures (in reflection) of lines drawn on sample I2 using various scanning speeds and laser beam widths. The incident power is 210 mW.

10 ms to 1 min, suggesting the NP growth occurs on a time scale smaller than 10 ms. The value of the power threshold strongly depends on the initial state of the sample and particularly on the density and size of Ag NPs. For example, this is between 60 mW and 90 mW for sample I2. The experiments reported below were carried out with powers greater than the threshold power, leading to the NP growth under static exposure.

With fixed power and beam width while moving the sample at a constant speed, the following surprising behavior is observed: silver NPs oxidize at low speed and grow at higher speed. Figure 2 shows an optical microscopy picture of lines drawn on sample I2 at various speeds for different laser beam sizes (different intensities because the incident power is fixed). Each line starts with a dot on the left-hand side and is 300 $\mu$m long. When there is only oxidation, the film color does not change significantly compared to the initial brown color of the film that can be observed between the bright lines in Figure 2. These brown lines are observed after the initial dots located in the bottom part of Figure 2. On the contrary, the sample color turns bright when NPs have grown. For each beam size, there is a speed threshold above which the film color changes dramatically (threshold is at 40, 40, 50, and 60−70 $\mu$m·s$^{-1}$ from the left to the right on Figure 2). This speed threshold thus separates two regimes. Below the threshold, NPs only oxidize during the beam passage, and above, NPs grow. One can note that when approaching the threshold value, as for the lowest speed of Figure 2 and the beam width 17.4 $\mu$m, a bright color can appear at the beginning of the line before vanishing during the laser scan. Such lines are not considered as bright lines. The initial dot that starts each line also appears when the shutter is open once the motor has reached a constant speed. The shutter opening immediately provides the maximum local intensity of the laser and hence the absence of any oxidation phenomenon. Thus, the initial size of silver nanoparticles in this dot is larger than the subsequent ones, which receive the maximal local intensity of the laser beam after oxidation and size reduction in the course of the laser scanning. Larger nanoparticles for a given intensity suggests a higher temperature raise. NP growth thus always occurs in the initial dot but does not hold when scanning the film if oxidation is sufficiently long.

This result is supported by TEM observations: Figure 3 reports HAADF-STEM micrographs of sample I2 in the initial state (Figure 3a) after laser scanning at a speed lower than the threshold (Figure 3b) or greater than the threshold (Figure 3c). Size histograms of the NPs distributions are plotted on the left part of each figure. They result from the measurement of around 15000 nanoparticles in 25 pictures recorded at different magnifications to accurately measure all sizes of particles. The smallest sizes were measured within an accuracy of ±0.1 nm. In Figure 3b the size distribution can be fitted by a single Gaussian function (red curve), while for (a) and (c), a good fit (red curve) requires the superposition of two Gaussian components (green and yellow curves). Sample I2 initially shows two distributions of NP size (Figure 3a). One is centered at 3 nm and corresponds to nanoparticles located near the film top surface (left-hand side of the gray area in Figure 3a), and the other is centered at 1.5 nm and corresponds to particles located in the rest of the film. The photocatalytic growth of NPs near the film top surface has already been reported and is due to the high absorption of TiO$_2$ in the UV.[32,38] Consistently, the smaller size distribution (green curve in Figure 3a) corresponds
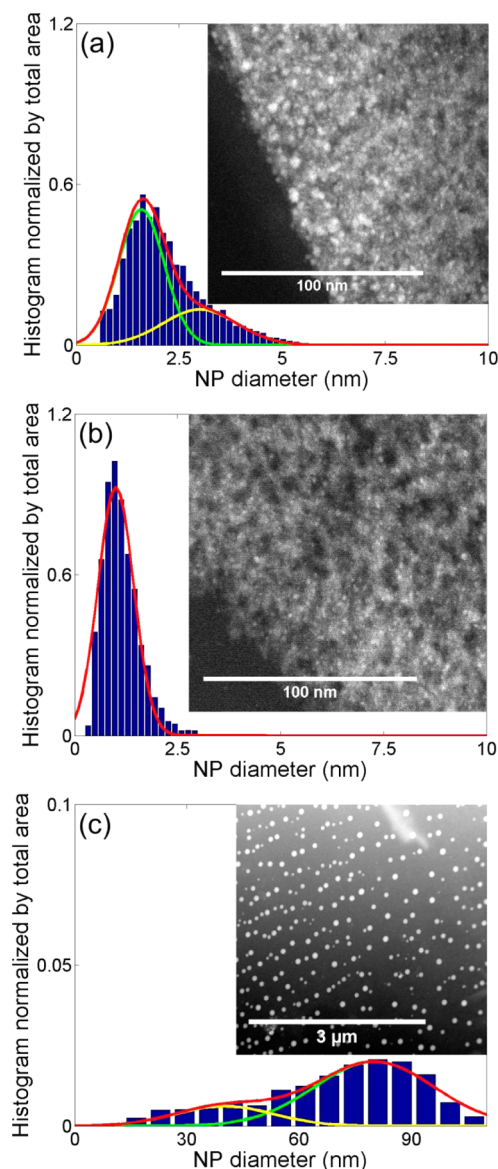


**Figure 3.** Typical HAADF-STEM micrographs and size histograms of sample I2 (a) in the initial state (sectional view), (b) after illumination at a scanning speed lower than the speed threshold (sectional view), and (c) after illumination at a scanning speed greater than the threshold (top view). The incident power is 150 mW and the beam size equals 22.9 $\mu$m.

typically to that found on sample I1, not exposed to UV light. After exposure, below the speed threshold, the average NP size always decreases, down to 1 nm as shown in Figure 3b, whereas there is a spectacular increase above the speed threshold, as illustrated in Figure 3c, where the average particle size is around 80 nm. HAADF-STEM characterizations clearly show, as reported earlier,[19] that Ag NPs keep a nearly spherical shape even at large diameter. It can also be noted that previous studies demonstrated that under certain exposure conditions (not detailed here) these grown NPs can self-organize along well-defined 1D gratings.[19,39] The work reported here focuses more on the formation mechanisms and not on self-organization, and hence we do not show NP gratings.

**Modeling the Physicochemical Mechanisms Resulting from Plasmon-Induced Charge Transfers.** We propose a model based on three main reactions to predict the changes in

the Ag nanoparticle size during exposure as a function of various exposure parameters and intrinsic parameters (Figure 4). Assuming that the initial samples contain three forms of
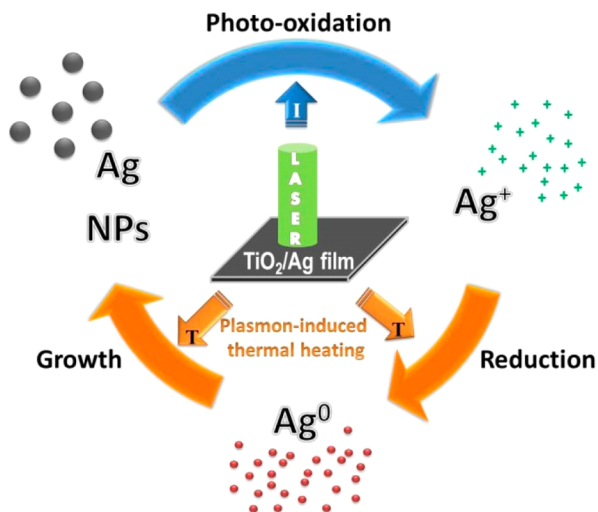


**Figure 4.** Illustration of the three main chemical reactions that control the distribution of silver between its three possible forms activated either directly by the laser intensity or by the plasmon-induced temperature increase.

silver: $Ag^0$, $Ag^+$, and Ag NPs, we consider an oxidation reaction that decreases the NPs size and increases the number of $Ag^+$ ions, a reduction reaction that converts $Ag^+$ to $Ag^0$, and a growth reaction that increases the size, while decreasing the density, of NPs from $Ag^0$ atoms. All these reactions are induced by laser light. The oxidation rate is proportional to the number of absorbed photons; the reduction and growth yields depend on the film temperature, whose increase results from the plasmon absorption of Ag NPs. The modeling of these reactions is described in the subsections below. It gives rise to three coupled differential equations, solutions to which are calculated by considering a time dependent intensity distribution with a Gaussian shape, whose temporal width depends on the beam diameter and the scanning speed.

*A. Oxidation.* The number of silver atoms oxidized per nanoparticle and per unit time is proportional to the number of absorbed photons per unit time and can be written as:

$$\text{Oxy}(t) = \frac{I(t)\sigma_{\text{abs}}(t)}{h\nu}\eta^- \tag{1}$$

where $h$ is the Planck constant, $\nu$ is the incident frequency, $I(t)$ the incident intensity varying in time at a given point during the laser scan, $\sigma_{\text{abs}}(t)$ the absorption cross-section of Ag NPs, and $\eta^-$ the ionization quantum efficiency of silver in titania. $I(t)$ can be written as $I(t) = P(t)(1-R(t))/(\pi r^2)$, where $P(t)$ is the incident power, $r$ is the laser beam radius, and $R(t)$ the total reflectivity of the sample taking into account multiple wave interferences within the $TiO_2$ film.[40] To calculate $R(t)$, the film is divided into two layers of equal thickness. The top layer contains NPs with a fixed size (the initial one), and the bottom one contains NPs whose size varies in time. This two-layer model is in line with previous results, which show that the final samples consist of a plane of NPs buried within the $TiO_2$ film near the film substrate interface.[19] This plane containing large silver NPs is covered with a thin layer of $TiO_2$ that may contain very small silver NPs. Experimental characterizations of films

suggest a thickness of 100 nm for each layer. The refractive index of each layer is deduced from the Maxwell−Garnett theory,[41] where a porous $TiO_2$ film of refractive index 1.7 is filled with silver NPs whose refractive index depends on their size and is calculated from the expression of the dielectric function of bulk silver corrected in size, taking into account the classical free path effect.[42] In addition, we have to take into account that the NP density of the bottom layer varies with the NP size as discussed later. The calculated refractive index and total reflectivity of the film are shown as a function of the NP diameter in Figure S1 of Supporting Information. $\sigma_{\text{abs}}(t)$ is calculated for each NP size using the Mie theory for spherical particles. $\eta^-$ has been estimated from experimental results where only oxidation occurs. This was performed by working with a laser power below the power threshold and measuring time variations of the sample transmittance.

*B. Reduction.* The growth of silver NPs is described by a two-step model adapted from ref 43, where silver ions are initially reduced to silver atoms, which diffuse to adsorb on silver NPs.

In this earlier work, the film thickness was higher than 1 $\mu$m and a depth dependent silver concentration was needed. Our layers, in contrast, are only 100 nm thick and are considered homogeneous at all times. The last assumption is to consider that the silver ion mobility is extremely high. We therefore write the number of $Ag^+$ ions reduced per unit time per unit volume as:

$$\text{red}(t) = p(t)D_{\text{red}}(t)C_{\text{red}}C_{Ag^+}^{2/3}(t)$$
$$= e^{-E_p/R_g T(t)} \cdot D_r e^{-E_D/R_g T(t)} C_{\text{red}} C_{Ag^+}^{2/3}(t) \tag{2}$$

where $D_{\text{red}}(t)$ and $C_{\text{red}}$ are the diffusion coefficient and the concentration of the reducing agent, respectively. $C_{Ag^+}$ is the concentration of $Ag^+$ ions, and $p$ is the probability of silver ions reduction. In our dynamic model, all quantities are written as time functions, although it is often indirect. This is the case for $p(t)$ and $D_{\text{red}}(t)$ that are actually only functions of the absolute film temperature $T(t)$, which varies in time. The temperature dependence of $p$ and $D_{\text{red}}$ can be reasonably described by the Arrhenius law, as written in eq 2, where $E_p$ and $E_D$ are activation energies and $R_g$ is the gas constant. The reducing agent is not clearly identified in our system; it may be atmospheric $H_2$, $TiO_2$ itself at high temperature, or even chemical compounds in the glass substrate. In any case, its concentration can reasonably be assumed to be constant. Specific experiments need to be carried out in the future to identify chemical species that contribute to the reduction of silver ions during laser exposure under high intensity. However, whatever the reducing agents involved in this reaction, eq 2 remains the same. To run numerical calculations, we will consider $D_r$ values close to the diffusion coefficient of $H_2$ in mesoporous systems at room temperature and for $E_D$ the activation energy of the reduction reaction of silver ions by $H_2$.

Equation 2 depends on temperature. The latter is calculated with the CW thermal model developed by Calder et al.[44] for a general multilayer structures, which has been applied here to our two-layer system on glass substrate described in the previous subsection. In this model, the absorption coefficient is supposed to be homogeneous under the laser beam. The analytical expression that is deduced in steady state is well suited in our case where a CW laser is used. Temperature is known to stabilize in the picosecond regime,[45] and the scanning

speeds used in these experiments are sufficiently slow so that the discretization time used for calculation of the steady state temperature is reached. In this model, the temperature rise upon laser exposure depends on the incident power $P(t)$, the beam radius $r$, the reflection coefficient of the sample $R(t)$, and the layers thickness; it also depends on the thermal conductivity of the different layers and their absorption coefficients. Thermal conductivities are assumed to be constant and are chosen in reasonable ranges of values for the nanocomposite layers or for the glass substrate. The film absorption coefficient is the product of the absorption cross-section $\sigma_{abs}(t)$ calculated for one NP and the NP density $C_{NP}$. $TiO_2$ is fully transparent at 488 nm wavelength and does not contribute to the film absorption.

The analysis of HAADF-STEM micrographs shows that the NP density depends strongly on the NP size. Table 1 gives

**Table 1. Average NP Density and Diameter Measured on Samples after Different Treatments**

| sample | av NP diameter (nm) | av NP density (m$^{-3}$) |
|---|---|---|
| I2 after NP oxidation | 1 | $9.7 \times 10^{23}$ |
| I1 initial state | 1.5 | $8.8 \times 10^{23}$ |
| I2 initial state | 3 | $4.7 \times 10^{23}$ |
| I2 after NP growth | 80 | $2.0 \times 10^{20}$ |

experimental values obtained after different treatments on samples I1 and I2, where the NP density can vary up to 4 orders of magnitude. This suggests that the NP density cannot be considered as constant during the size variations of NPs, i.e., as a function of time. An empirical law is proposed to fit the experimental data. This law corresponds to a linear variation of the interparticle distance with the NP size. It leads to the following relation between the NP density $C_{NP}$ and the NP radius $R_{NP}$:

$$C_{NP}(t) = 1/(mR_{NP}(t) + n)^3 \qquad (3)$$

where coefficients $m$ and $n$ are fitted from values of Table 1 to 2.6 and $8.7 \times 10^{-9}$, respectively.

In the next section, we model the growth of silver NPs by considering the adsorption of silver atoms on the growing NPs. We introduced eq 3 in the model to account for coalescence and we forced the theoretical density of NPs to decrease when the NP radius increases. Coalescence is indeed expected to occur during the laser irradiation. The reaction temperature during the laser scan can exceed the crystallization temperature of $TiO_2$ in the anatase (>700 K) or rutile (>1000 K) phase depending on the exposure conditions.[19,31] The melting point of silver is 1233 K, but this temperature drastically decreases when the radius of Ag NPs becomes low, <850 K for a NP diameter of 3 nm, and around 680 K for a 2 nm diameter.[46] The Tammann temperature is approximately half the melting point, <425 K for NP smaller than 3 nm. Hence, the reaction temperature is indeed expected to be higher than the Tammann temperature of silver NPs. Bulk atoms tend to move when the Tammann temperature is reached, which leads to interparticle diffusion and therefore coalescence of metal particles.[47]

*C. Growth.* Once reduced, silver atoms adsorb on Ag NPs leading to the NPs growth. The solubility $S$ of $Ag^0$ is very low, and the $TiO_2$ matrix is rapidly oversaturated. $Ag^0$ atoms diffuse and contribute to the growth of NPs they encounter provided that their radius $R_{NP}$ is larger than the radius of the critical nucleus under which NPs spontaneously redissolve due to

thermodynamic reasons. As $S$ is very small, the radius of the critical nucleus is actually comparable with the atomic size.[43] It is then possible to show that the local $Ag^0$ flow to the surface of a NP of radius $R_{NP}$ is given by:[43]

$$J_{Ag^0}(t) = D_{Ag^0}(t) \frac{C_{Ag^0}(t) - c_R(t)}{R_{NP}(t)}$$

$$= D_0 e^{-E_{D_0}/R_g T(t)} \frac{C_{Ag^0}(t) - c_R(t)}{R_{NP}(t)} \qquad (4)$$

where $D_{Ag^0}(t)$ and $C_{Ag^0}(t)$ are the diffusion coefficient and the concentration of neutral silver, respectively. As for other atomic or ionic species, the diffusion coefficient of $Ag^0$ varies with temperature according to the Arrhenius law. The critical concentration $c_R(t)$ at the surface of the NP is given by:

$$c_R(t) = S\left(1 + \frac{2\gamma\omega}{k_B T(t) R_{NP}(t)}\right) \qquad (5)$$

with $\gamma$ the interface tension between the Ag NP and the matrix and $\omega$ the atomic volume of Ag in a NP. For fcc crystals, $\omega = a^3/4$, with the lattice parameter of silver $a$ equal to 0.4086 nm. $k_B$ is the Boltzmann constant.

Finally, the number of silver atoms adsorbed on one NP per unit time can be written as:

$$grw(t) = 4\pi R_{NP}^2(t) J_{Ag^0}(t) \qquad (6)$$

*D. Three Coupled Differential Equations.* We can now deduce the differential equations describing the variations of the number of silver atoms in each form: $Ag^+$, $Ag^0$, and Ag NP.

The number of silver atoms, $N_{Ag1NP}$, in a NP of radius $R_{NP}$ varies according to the following equation:

$$\frac{dN_{Ag_{1NP}}(t)}{dt} = (grw(t) - oxy(t)) \qquad (7)$$

And because $N_{Ag_{1NP}}(t) = 4\pi R_{NP}^3(t)/3\omega$, the variation of the NP radius with respect to time is governed by:

$$\frac{dR_{NP}(t)}{dt} = \frac{\omega}{4\pi R_{NP}^2(t)}(grw(t) - oxy(t)) \qquad (8)$$

The variation of the number of silver atoms included in NPs per unit volume, $C_{AgNP}$, can then be expressed as a function of the NP density as:

$$\frac{dC_{Ag_{NP}}(t)}{dt} = \frac{d(C_{NP}(t)N_{Ag_{1NP}}(t))}{dt}$$

$$\frac{dC_{Ag_{NP}}(t)}{dt} = C_{NP}(t)\frac{dN_{Ag_{1NP}}(t)}{dt} + N_{Ag_{1NP}}(t)\frac{dC_{NP}(t)}{dt} \qquad (9)$$

The second term in the right-hand part of eq 9 can be simplified as follows:

$$N_{Ag_{1NP}}(t)\frac{dC_{NP}(t)}{dt} = N_{Ag_{1NP}}(t)\frac{dC_{NP}(t)}{dR_{NP}(t)}\frac{dR_{NP}(t)}{dt}$$

$$N_{Ag_{1NP}}(t)\frac{dC_{NP}(t)}{dt} = \frac{R_{NP}(t)}{3}\frac{dC_{NP}(t)}{dR_{NP}(t)}(grw(t) - oxy(t)) \qquad (10)$$

so we have

$$\frac{dC_{Ag_{NP}}(t)}{dt} = \left(C_{NP}(t) + \frac{R_{NP}(t)}{3}\frac{dC_{NP}(t)}{dR_{NP}(t)}\right)$$
$$(grw(t) - oxy(t)) \tag{11}$$

Oxidation turns the silver atoms included in NPs into $Ag^+$ ions, but the reduction transforms $Ag^+$ into free neutral silver atom. So the variation in the $Ag^+$ ions concentration can be given by:

$$\frac{d}{dt}C_{Ag^+}(t) = -red(t)$$
$$+ \left(C_{NP}(t) + \frac{R_{NP}(t)}{3}\frac{dC_{NP}(t)}{dR_{NP}(t)}\right)oxy(t) \tag{12}$$

And similarly, we can also get the variation of the free neutral Ag atom concentration as:

$$\frac{d}{dt}C_{Ag^0}(t) = red(t) - grw(t)\left(C_{NP}(t) + \frac{R_{NP}(t)}{3}\frac{dC_{NP}(t)}{dR_{NP}(t)}\right) \tag{13}$$

The three-dimensional ordinary differential equations system (ODE system) represented by eqs 8 12, and 13 is solved using Matlab.

*E. Parameters Used in the Simulations.* Certain parameters of the model have no significant influence on the simulation results. This is the case for the solubility $S$ and the element $2\gamma\omega/TR_{NP}$ except when the $Ag^0$ concentration becomes very low. According to ref 43, the solubility $S$ should be negligible compared to the $Ag^0$ concentration and has been estimated to be $10^4$ times smaller than $Ag^0$ concentration. $2\gamma\omega/TR$ at 500 K is set equal to 2.5 nm. The diffusion coefficient of $H_2$ and its concentration do not significantly influence the simulated results. In the literature,[48-50] the activation energy of $H_2$ diffusion is found to range from 0.0024 to 0.05 eV and the diffusion coefficient is reported to vary from $5 \times 10^{-15}$ to $2.5 \times 10^{-14}$ m$^2$·s$^{-1}$. The activation energy of the reduction reaction probability is chosen at about $0.7 \times 10^{-19}$ J, as in the work of Kaganovskii et al.;[43] it has however no significant influence.

The neutral silver atom diffusion coefficient, the metallic ionization quantum efficiency $\eta^-$, and the initial concentration of $Ag^+$ and $Ag^0$ have an important influence on the simulation results. It is difficult to find the activation energies of different processes in mesoporous $TiO_2$ film in the literature because they depend largely on film porosity, but a reasonable value range can be chosen from the activation energy in similar materials. In refs 51,52, the activation energy of $Ag^0$ diffusion is around 1 eV, so we can consider a reasonable value range from 0.5 to 1.5 eV. The diffusion coefficient at 500 K can range from $5 \times 10^{-17}$ to $1 \times 10^{-14}$ m$^2$·s$^{-1}$. The ionization quantum efficiency of metal, $\eta^-$, was estimated to be $1.3 \times 10^{-6}$ for sample I1 and $2.3 \times 10^{-6}$ for sample I2. This value can slightly vary from one sample to another, especially due to small variations in the average size of the film porosity. On films with smaller pore diameters, it can go down to $1 \times 10^{-9}$ as estimated from previous studies in which only oxidation occurred.[35] In the initial state, $Ag^0$ concentration should be at least $1.2 \times 10^{28}$ m$^{-3}$, and for $Ag^+$, the concentration has been estimated at about $0.6 \times 10^{28}$ m$^{-3}$.

**Comparing Simulated and Experimental Results.** The resolution of the ODE system gives the time variations of the NP radius during the laser passage. When changing the scanning speed, we change the temporal width of the Gaussian

function describing the variations of the beam intensity versus time at a given point of the sample (dotted lines in Figure 5).
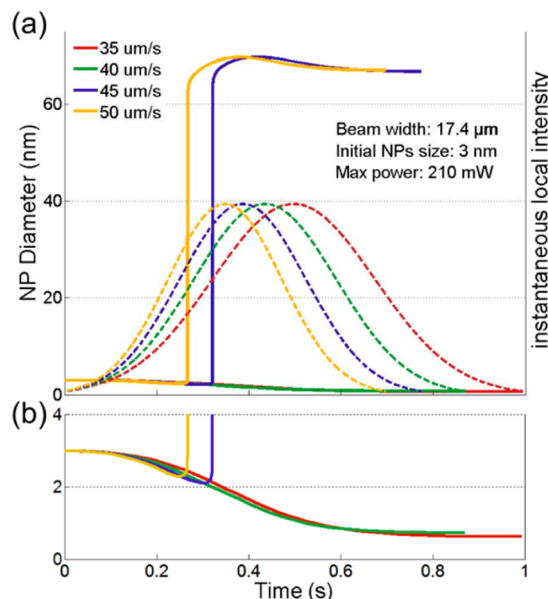


**Figure 5.** Simulation results. (a) Variations of the NPs size (continuous lines) and instantaneous local intensity (dotted lines) versus time for different scanning speeds. (b) Zoom on the bottom part of (a).

Figure 5 shows that the scanning speed greatly influences the final NP size (the total reflectivity of the film versus time is also shown in Figure S2 of Supporting Information). As for the experimental results shown in Figures 2 and 3, the final NP size is lower than the initial one at speeds lower than a threshold value, here between 40 and 45 $\mu$m·s$^{-1}$, and is much greater than the initial one at higher speed. Simulations better inform about the kinetics of oxidation and growth reactions. When the NP growth occurs (at speeds higher than the threshold), it leads to a sharp increase in the NPs size that tends to saturate due to the limited number of silver atoms in the system and the equilibrium reached between the "grw" and "oxy" terms (see eq 8). The presence of a speed threshold can be explained in the following manner. Oxidation is proportional to the absorbed number of photons. It therefore increases with the instantaneous local intensity and with the absorption cross-section of Ag NPs (the latter is not a uniform function of $R_{NP}$; according to Mie theory, it increases with the NP size until $R_{NP} = 21.5$ at 488 nm wavelength, then decreases). Oxidation occurs whatever the incident intensity and starts decreasing the NPs size from the very beginning of the beam passage. During the laser scan, the instantaneous local incident intensity increases and the NPs size decreases. Depending on the speed at which the NP size decreases when the intensity increases, the resulting temperature can either increase or decrease. As the reduction and NP growth reactions depend on the temperature in an exponential way, the temperature elevation adds to the effect of the increasing incident power and tends to abruptly increase the growth rate. The changes in the temperature rise during the laser passage, and their effect on the surrounding matrix will be described elsewhere.

In sum, when the speed is low, oxidation lasts longer and decreases the NP size at a value small enough to inhibit any significant temperature increase in the NP during the laser

beam passage. In this case, even at the highest laser intensity, oxidation predominates over growth. On the contrary, when the speed increases, the laser intensity increases rapidly enough to encounter less oxidized NPs, i.e., larger NPs, which creates a large temperature increase in the film and rapidly boosts the NP growth. Simulations from Figure 5 indicate that the growth of NPs always starts at the rising edge of the laser intensity and completes before the laser intensity starts decreasing. The self-stabilization of the nanoparticle size mainly results from the size dependence of the absorption cross-section for spherical NPs. Once the latter starts decreasing from a NP radius of ~22 nm (Mie theory for Ag spheres in $TiO_2$), the temperature rise rapidly decreases and the growth kinetics slows down up to vanish when the NP size is too high and the temperature rise too low. This surprisingly fast predicted jump comes from the nonlinear and nested features of the equations. Although we succeeded in obtaining a simple set of three differential equations, they are highly nonlinear through exponential and power dependencies and also include feedback mechanisms. For instance, in the presence of NPs, laser illumination induces absorption, hence temperature increase, NPs growth, and again, absorption increases. These two key ingredients give rise to the rich and complex predicted and observed behavior that is dependent on experimental conditions.

To verify the relevance of the developed model, we performed other comparisons with experimental results by varying parameters that have major influences on the speed threshold. These parameters are the initial state of the film characterized by the original Ag NP size, the incident laser power, and the width of the laser beam. Experimental and simulation results are gathered in Figures 6 and 7, respectively, and they show the changes in the speed threshold as a function
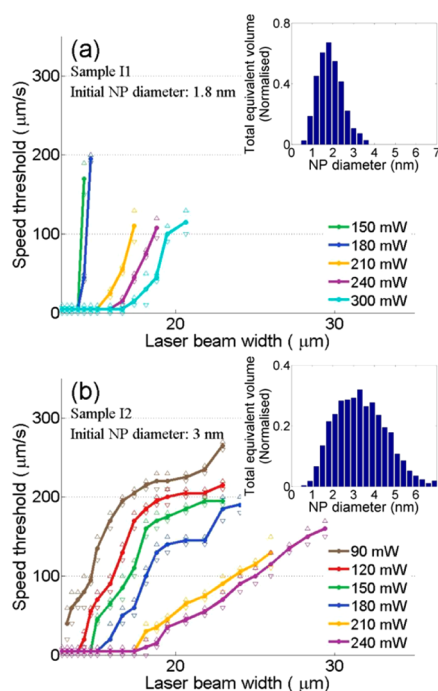


**Figure 7.** Simulated speed threshold versus laser beam width for several incident powers and two initial NPs sizes: (a) corresponds to an initial NP diameter of 1.8 nm and (b) to an initial NP diameter of 3 nm.

of these parameters. The experimental and simulated curves exhibit similar trends that can be understood from physical interpretations.

For a given beam width, the speed threshold increases when the incident power decreases. With a lower laser power, the temperature reached for a given speed is lower. We need to increase the scanning speed to shorten oxidation and get larger NP size before reaching the maximum intensity to observe the NP growth.

For a given power, the speed threshold increases when the beam diameter increases. This corresponds to a decrease in intensity as in the previous case and can be interpreted similarly. However, the temperature increase is not proportional to the intensity. As described in ref44, temperature is proportional to the incident power and varies as a complex function of the beam diameter. So, two different couples of power and beam width corresponding to the same intensity do not provide the same temperature rise and hence do not lead to the same speed threshold.

Considering the initial NP size, sample I2 exhibits two size distributions centered on 1.5 and 3 nm, respectively (Figure 3a). The sample temperature is strongly dependent on both the absorption cross-section varying with the NP size and the NP density. Between the two measured size distributions, the density does not vary enormously and only the size significantly influences the plasmon-induced temperature rise at the beginning of the rising intensity edge. More than the NP size, it is the NP volume that is the significant parameter that



**Figure 6.** Experimental speed threshold versus laser beam width for several incident powers and two initial NPs sizes: (a) corresponds to sample I1 and (b) to sample I2. Open triangles show the measurement uncertainty. Inset in each graph shows the histogram of the normalized total equivalent volume per NP diameter calculated from HAADF-STEM pictures in the initial state for each sample.
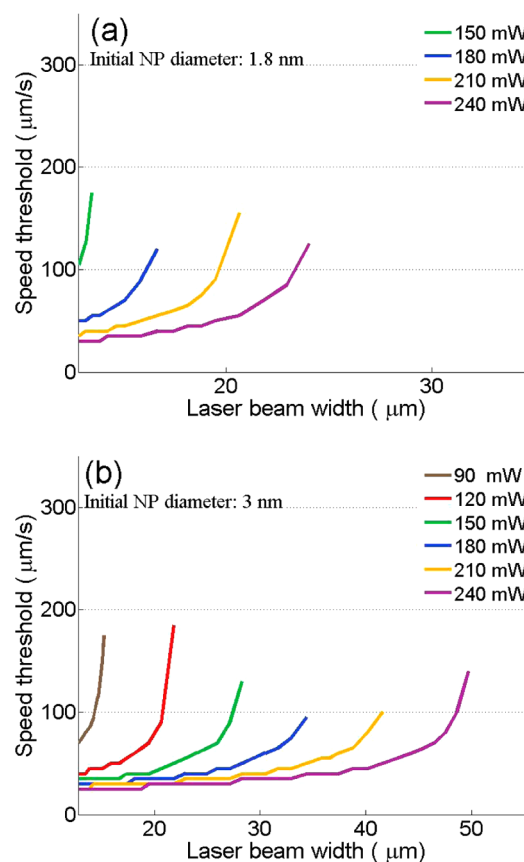
has to be considered here. For very small NPs, the absorption cross-section given by the Mie theory simplifies in the quasistatic approximation to be directly proportional to the NP volume.[40] As the model does not consider a size distribution but only an average NP size, it is appropriate to consider as the initial NP size, the one that imposes the temperature, i.e., the one with the maximum equivalent volume. Histograms giving the total equivalent volume versus the NP diameter for both initial samples are shown in the inset in Figure 6. They justify the use of an average initial diameter of 1.8 or 3 nm for simulations of sample I1 or I2, respectively.

Comparing the results obtained for two different initial NP sizes, we observe that the power threshold required to induce the NPs growth is lower when the initial NP size is higher. This results from the fact that the temperature increases with the NP size. Also, the NP growth can be observed for larger beam sizes, whatever the power used, when the initial NPs are bigger. For a given couple of power and beam width, the speed threshold is lower for a higher initial NP size. This is required to extend the oxidation time (by reducing the speed) to get small NPs so as not to reach the temperature leading to the NPs growth when their initial size is larger.

Theoretical curves all exhibit an exponential growth when the laser width approaches the maximum value leading to the NP growth. This is also the case for sample I1, where the size distribution is narrow. For a given laser power, the incident intensity decreases when enlarging the beam and the time needed to reach the instantaneous local intensity, giving rise to the NP growth increases. The laser scan must be sped up to counteract the fact that the beam is wider and the required intensity is closer to the beam center. Moreover, when intensity approaches the threshold, the temperature rise becomes quite sensitive to the NP size and oxidation must be significantly shortened. However, the experimental growth of the speed threshold versus the laser beam width is less sharp for sample I2 than calculated. This difference is attributed to the broader size distribution of sample I2, which is not taken into account in the model where only one NP size is considered. NPs larger than 3 nm that are present in the sample can activate the growth process even at larger beam width than the ones predicted in Figure 7. A useful improvement of the model will be to consider size distributions of Ag NPs.

Finally, we note that the calculated speed threshold ranges are in very good agreement with the experimental ones for the same values of varying parameters. All the fitted parameters are close to values found in the literature. This model appears therefore to be quite relevant for the study of coupled chemical reactions resulting from plasmon-induced charge transfers in Ag:TiO$_2$ systems despite a number of approximations, most notably that we consider only one NP size at each time $t$. We also know that crystalline phase changes of TiO$_2$ and a collapse of the matrix mesoporosity occur during the NP growth due to the high temperature rise.[19,31] These major events influence the thermal, optical, and chemical properties of the material and could change the final predicted NP size when growth becomes predominant. However, they will not change the way both mechanisms compete at the initiation of the chemical reaction.

## CONCLUSIONS

In this paper, we characterized and modeled the main physicochemical mechanisms that influence the size of Ag NPs in TiO$_2$ matrices loaded with Ag$^+$, Ag$^0$ and Ag NPs when exposed to visible light. Provided that incident intensity is high enough, oxidation competes with growth. Oxidation directly depends on the number of photons absorbed by silver NPs due to their LSPR. The growth, which results from a two-step process, is promoted by the plasmon-induced temperature increase and varies in a strong nonlinear manner with the laser intensity. For a given couple of incident power and beam width, the relative importance of both reactions can be tuned by the scanning speed of the laser beam on the sample surface. This results from the nonuniform intensity profile of the laser beam. Oxidation occurs whatever the intensity and increases linearly with it with a relatively slow kinetics. On the contrary, growth only becomes significant above a certain threshold temperature reached for a combination of a high intensity and large NP size (or high enough absorption cross-section) and is relatively rapid. This gives rise to two distinct regimes where (1) oxidation outweighs and the final NP size is smaller than the initial one after the beam passage and (2) growth outweighs and the final NP size is larger (in our case much larger) than the initial one. These two regimes happen below and above a speed threshold, respectively. The speed threshold appears to increase with the beam width and to decrease when the incident power and the initial NP size increase, as observed experimentally and predicted by simulations. The proposed model, as well as the laser process presented to control the NPs size, would be useful to design and produce devices for photocatalysis and photovoltaic applications.

## ASSOCIATED CONTENT

**Ⓢ Supporting Information**

Graphs of the refractive index and total reflectivity of the TiO$_2$/Ag layer in function of the Ag NP size or time. This material is available free of charge via the Internet at http://pubs.acs.org.

## AUTHOR INFORMATION

**Corresponding Authors**

*Email: nathalie.destouches@univ-st-etienne.fr .
*Email: guy.vitrant@minatec.grenoble-inp.fr.

**Notes**

The authors declare no competing financial interest.

## ACKNOWLEDGMENTS

## REFERENCES

(1) Tian, Y.; Tatsuma, T. Mechanisms and Applications of Plasmon-Induced Charge Separation at TiO$_2$ Films Loaded with Gold Nanoparticles. *J. Am. Chem. Soc.* **2005**, *127*, 7632−7637.

(2) Tian, Y.; Tatsuma, T. Plasmon-Induced Photoelectrochemistry at Metal Nanoparticles Supported on Nanoporous TiO$_2$. *Chem. Commun.* **2004**, *16*, 1810.

(3) Clavero, C. Plasmon-Induced Hot-Electron Generation at Nanoparticle/metal-Oxide Interfaces for Photovoltaic and Photo-catalytic Devices. *Nature Photonics* **2014**, *8*, 95−103.

(4) Zhou, W.; Li, T.; Wang, J.; Qu, Y.; Pan, K.; Xie, Y.; Tian, G.; Wang, L.; Ren, Z.; Jiang, B.; et al. Composites of Small Ag Clusters Confined in the Channels of Well-Ordered Mesoporous Anatase TiO2 and Their Excellent Solar-Light-Driven Photocatalytic Performance. *Nano Res.* **2014**, *7*, 731−742.

(5) Kowalska, E.; Mahaney, O. O. P.; Abe, R.; Ohtani, B. Visible-Light-Induced Photocatalysis through Surface Plasmon Excitation of Gold on Titania Surfaces. *Phys. Chem. Chem. Phys.* **2010**, *12*, 2344−2355.

(6) Kowalska, E.; Abe, R.; Ohtani, B. Visible Light-Induced Photocatalytic Reaction of Gold-Modified Titanium(IV) Oxide Particles: Action Spectrum Analysis. *Chem. Commun.* **2009**, *No. 2*, 241−243.

(7) Gomes Silva, C.; Juárez, R.; Marino, T.; Molinari, R.; García, H. Influence of Excitation Wavelength (UV or Visible Light) on the Photocatalytic Activity of Titania Containing Gold Nanoparticles for the Generation of Hydrogen or Oxygen from Water. *J. Am. Chem. Soc.* **2011**, *133*, 595−602.

(8) Ingram, D. B.; Christopher, P.; Bauer, J. L.; Linic, S. Predictive Model for the Design of Plasmonic Metal/Semiconductor Composite Photocatalysts. *ACS Catal.* **2011**, *1*, 1441−1447.

(9) Gong, D.; Ho, W. C. J.; Tang, Y.; Tay, Q.; Lai, Y.; Highfield, J. G.; Chen, Z. Silver Decorated Titanate/Titania Nanostructures for Efficient Solar Driven Photocatalysis. *J. Solid State Chem.* **2012**, *189*, 117−122.

(10) Grätzel, M. Photoelectrochemical Cells. *Nature* **2001**, *414*, 338−344.

(11) Nakamura, E.; Kogo, A.; Sakai, N.; Tatsuma, T. Gold Cluster/Titanium Dioxide Heterojunction Photovoltaic Cell. *Appl. Phys. Lett.* **2014**, *105*, 083113.

(12) Sakai, N.; Fujiwara, Y.; Takahashi, Y.; Tatsuma, T. Plasmon-Resonance-Based Generation of Cathodic Photocurrent at Electro-deposited Gold Nanoparticles Coated with TiO₂ Films. *ChemPhysChem* **2009**, *10*, 766−769.

(13) Valverde-Aguilar, G.; García-Macedo, J. A.; Rentería-Tapia, V.; Aguilar-Franco, M. Photoconductivity Studies on Amorphous and Crystalline TiO₂ Films Doped with Gold Nanoparticles. *Appl. Phys. A: Mater. Sci. Process.* **2011**, *103*, 659−663.

(14) Sakai, N.; Sasaki, T.; Matsubara, K.; Tatsuma, T. Layer-by-Layer Assembly of Gold Nanoparticles with Titania Nanosheets: Control of Plasmon Resonance and Photovoltaic Properties. *J. Mater. Chem.* **2010**, *20*, 4371−4378.

(15) Chen, K.; Feng, X.; Hu, R.; Li, Y.; Xie, K.; Li, Y.; Gu, H. Effect of Ag Nanoparticle Size on the Photoelectrochemical Properties of Ag Decorated TiO₂ Nanotube Arrays. *J. Alloys Compd.* **2013**, *554*, 72−79.

(16) Yu, K.; Tian, Y.; Tatsuma, T. Size Effects of Gold Nanaoparticles on Plasmon-Induced Photocurrents of Gold-TiO₂ Nanocomposites. *Phys. Chem. Chem. Phys.* **2006**, *8*, 5417−5420.

(17) Govorov, A. O.; Zhang, H.; Gun'ko, Y. K. Theory of Photoinjection of Hot Plasmonic Carriers from Metal Nanostructures into Semiconductors and Surface Molecules. *J. Phys. Chem. C* **2013**, *117*, 16616−16631.

(18) Atwater, H. A.; Polman, A. Plasmonics for Improved Photovoltaic Devices. *Nature Mater.* **2010**, *9*, 205−213.

(19) Destouches, N.; Crespo-Monteiro, N.; Vitrant, G.; Lefkir, Y.; Reynaud, S.; Epicier, T.; Liu, Y.; Vocanson, F.; Pigeon, F. Self-Organized Growth of Metallic Nanoparticles in a Thin Film under Homogeneous and Continuous-Wave Light Excitation. *J. Mater. Chem. C* **2014**, *2*, 6256−6263.

(20) Sönnichsen, C.; Franzl, T.; Wilk, T.; von Plessen, G.; Feldmann, J.; Wilson, O.; Mulvaney, P. Drastic Reduction of Plasmon Damping in Gold Nanorods. *Phys. Rev. Lett.* **2002**, *88*, 077402.

(21) Lehmann, J.; Merschdorf, M.; Pfeiffer, W.; Thon, A.; Voll, S.; Gerber, G. Surface Plasmon Dynamics in Silver Nanoparticles Studied by Femtosecond Time-Resolved Photoemission. *Phys. Rev. Lett.* **2000**, *85*, 2921−2924.

(22) Knight, M. W.; Wang, Y.; Urban, A. S.; Sobhani, A.; Zheng, B. Y.; Nordlander, P.; Halas, N. J. Embedding Plasmonic Nanostructure Diodes Enhances Hot Electron Emission. *Nano Lett.* **2013**, *13*, 1687−1692.

(23) White, T. P.; Catchpole, K. R. Plasmon-Enhanced Internal Photoemission for Photovoltaics: Theoretical Efficiency Limits. *Appl. Phys. Lett.* **2012**, *101*, 073905.

(24) Moskovits, M. Hot Electrons Cross Boundaries. *Science* **2011**, *332*, 676−677.

(25) Kawahara, K.; Suzuki, K.; Ohko, Y.; Tatsuma, T. Electron Transport in Silver-Semiconductor Nanocomposite Films Exhibiting Multicolor Photochromism. *Phys. Chem. Chem. Phys.* **2005**, *7*, 3851−3855.

(26) Ohko, Y.; Tatsuma, T.; Fujii, T.; Naoi, K.; Niwa, C.; Kubota, Y.; Fujishima, A. Multicolour Photochromism of TiO₂ Films Loaded with Silver Nanoparticles. *Nature Mater.* **2003**, *2*, 29−31.

(27) Naoi, K.; Ohko, Y.; Tatsuma, T. TiO₂ Films Loaded with Silver Nanoparticles: Control of Multicolor Photochromic Behavior. *J. Am. Chem. Soc.* **2004**, *126*, 3664−3668.

(28) Nadar, L.; Destouches, N.; Crespo-Monteiro, N.; Sayah, R.; Vocanson, F.; Reynaud, S.; Lefkir, Y.; Capoen, B. Multicolor Photochromism of Silver-Containing Mesoporous Films of Amorphous or Anatase TiO₂. *J. Nanopart. Res.* **2013**, *15*, 1−10.

(29) Crespo-Monteiro, N.; Destouches, N.; Nadar, L.; Reynaud, S.; Vocanson, F.; Michalon, J. Y. Irradiance Influence on the Multicolor Photochromism of Mesoporous TiO₂ Films Loaded with Silver Nanoparticles. *Appl. Phys. Lett.* **2011**, *99*, 173106.

(30) Inagaki, T.; Goudonnet, J. P.; Little, J. W.; Arakawa, E. T. Photoacoustic Study of Plasmon-Resonance Absorption in a Bigrating. *J. Opt. Soc. Am. B* **1985**, *2*, 433−439.

(31) Crespo-Monteiro, N.; Destouches, N.; Saviot, L.; Reynaud, S.; Epicier, T.; Gamet, E.; Bois, L.; Boukenter, A. One-Step Micro-structuring of TiO₂ and Ag-TiO₂ Films by Continuous Wave Laser Processing in the UV and Visible Ranges. *J. Phys. Chem. C* **2012**, *116*, 26857−26864.

(32) Crespo-Monteiro, N.; Destouches, N.; Epicier, T.; Balan, L.; Vocanson, F.; Lefkir, Y.; Michalon, J.-Y. Changes in the Chemical and Structural Properties of Nanocomposite Ag:TiO₂ Films During Photochromic Transitions. *J. Phys. Chem. C* **2014**, *118*, 24055−24061.

(33) Crespo-Monteiro, N.; Destouches, N.; Fournel, T. Updatable Random Texturing of Ag/TiO₂ Films for Goods Authentication. *Appl. Phys. Express* **2012**, *5*, 075803.

(34) Nadar, L.; Sayah, R.; Vocanson, F.; Crespo-Monteiro, N.; Boukenter, A.; Joao, S. S.; Destouches, N. Influence of Reduction Processes on the Colour and Photochromism of Amorphous Mesoporous TiO₂ Thin Films Loaded with a Silver Salt. *Photochem. Photobiol. Sci.* **2011**, *10*, 1810−1816.

(35) Crespo-Monteiro, N.; Destouches, N.; Bois, L.; Chassagneux, F.; Reynaud, S.; Fournel, T. Reversible and Irreversible Laser Micro-inscription on Silver-Containing Mesoporous Titania Films. *Adv. Mater.* **2010**, *22*, 3166−3170.

(36) Epicier, T.; Sato, K.; Tournus, F.; Konno, T. Chemical Composition Dispersion in Bi-metallic Nanoparticles: Semi-Auto-mated Analysis Using HAADF-STEM. *J. Nanopart. Res.* **2012**, *14*, 1−10.

(37) Treacy, M. M. J.; Rice, S. B. Catalyst Particle Sizes from Rutherford Scattered Intensities. *J. Microsc.* **1989**, *156*, 211−234.

(38) Destouches, N.; Battie, Y.; Crespo-Monteiro, N.; Chassagneux, F.; Bois, L.; Bakhti, S.; Vocanson, F.; Toulhoat, N.; Moncoffre, N.; Epicier, T. Photo-Directed Organization of Silver Nanoparticles in Mesostructured Silica and Titania Films. *J. Nanopart. Res.* **2013**, *15*, 1−10.

(39) Destouches, N.; Martínez-García, J.; Hébert, M.; Crespo-Monteiro, N.; Vitrant, G.; Liu, Z.; Trémeau, A.; Vocanson, F.; Pigeon, F.; Reynaud, S.; et al. Dichroic Colored Luster of Laser-Induced Silver Nanoparticle Gratings Buried in Dense Inorganic Films. *J. Opt. Soc. Am. B* **2014**, *31*, C1−C7.

(40) Born, M.; Wolf, E.; Bhatia, A. B.; Clemmow, P. C.; Gabor, D.; Stokes, A. R.; Taylor, A. M.; Wayman, P. A.; Wilcock, W. L. *Principles*

of Optics: Electromagnetic Theory of Propagation, Interference and Diffraction of Light, 7th ed.; Cambridge University Press: Cambridge; New York, 1999.

(41) Garnett, J. C. M. Colours in Metal Glasses and in Metallic Films. *Philos. Trans. R. Soc. London, A* **1904**, *203*, 385−420.

(42) Battie, Y.; Destouches, N.; Bois, L.; Chassagneux, F.; Tishchenko, A.; Parola, S.; Boukenter, A. Growth Mechanisms and Kinetics of Photoinduced Silver Nanoparticles in Mesostructured Hybrid Silica Films Under UV and Visible Illumination. *J. Phys. Chem. C* **2010**, *114*, 8679−8687.

(43) Kaganovskii, Y.; Lipovskii, A.; Rosenbluh, M.; Zhurikhina, V. Formation of Nanoclusters Through Silver Reduction in Glasses: The Model. *J. Non-Cryst. Solids* **2007**, *353*, 2263−2271.

(44) Calder, I. D.; Sue, R. Modeling of CW Laser Annealing of Multilayer Structures. *J. Appl. Phys.* **1982**, *53*, 7545−7550.

(45) Von der Linde, D.; Sokolowski-Tinten, K.; Bialkowski, J. Laser−Solid Interaction in the Femtosecond Time Regime. *Appl. Surf. Sci.* **1997**, *109−110*, 1−10.

(46) Luo, W.; Hu, W.; Xiao, S. Size Effect on the Thermodynamic Properties of Silver Nanoparticles. *J. Phys. Chem. C* **2008**, *112*, 2359−2369.

(47) Sun, J.; Ma, D.; Zhang, H.; Liu, X.; Han, X.; Bao, X.; Weinberg, G.; Pfänder, N.; Su, D. Toward Monodispersed Silver Nanoparticles with Unusual Thermal Stability. *J. Am. Chem. Soc.* **2006**, *128*, 15756−15764.

(48) Torresi, R. M.; Cámara, O. R.; De Pauli, C. P.; Giordano, M. C. Hydrogen Evolution Reaction on Anodic Titanium Oxide Films. *Electrochim. Acta* **1987**, *32*, 1291−1301.

(49) Battisti, A.; Taioli, S.; Garberoglio, G. Zeolitic Imidazolate Frameworks for Separation of Binary Mixtures of $CO_2$, $CH_4$, $N_2$ and $H_2$: A Computer Simulation Investigation. *Microporous Mesoporous Mater.* **2011**, *143*, 46−53.

(50) Haran, B. S.; Popov, B. N.; White, R. E. Determination of the Hydrogen Diffusion Coefficient in Metal Hydrides by Impedance Spectroscopy. *J. Power Sources* **1998**, *75*, 56−63.

(51) McBrayer, J. D.; Swanson, R. M.; Sigmon, T. W. Diffusion of Metals in Silicon Dioxide. *J. Electrochem. Soc.* **1986**, *133*, 1242−1246.

(52) Butrymowicz, D. B.; Manning, J. R.; Read, M. E. Diffusion in Copper and Copper Alloys, Part II. Copper−Silver and Copper−Gold Systems. *J. Phys. Chem. Ref. Data* **1974**, *3*, 527−602.